

A Comparative Study of Image Restoration Networks for General Backbone Network Design

Xiangyu Chen^{1,2,3} * Zheyuan Li³ * Yuandong Pu^{2,4} * Yihao Liu²
Jiantao Zhou¹ Yu Qiao^{2,3} Chao Dong^{2,3}

¹University of Macau ²Shanghai Artificial Intelligence Laboratory

³Shenzhen Institutes of Advanced Technology, CAS ⁴Shanghai Jiao Tong University

<https://github.com/Andrew0613/X-Restormer>

Abstract

Despite the significant progress made by deep models in various image restoration tasks, existing image restoration networks still face challenges in terms of task generality. An intuitive manifestation is that networks which excel in certain tasks often fail to deliver satisfactory results in others. To illustrate this point, we select five representative image restoration networks and conduct a comparative study on five classic image restoration tasks. First, we provide a detailed explanation of the characteristics of different image restoration tasks and backbone networks. Following this, we present the benchmark results and analyze the reasons behind the performance disparity of different models across various tasks. Drawing from this comparative study, we propose that a general image restoration backbone network needs to meet the functional requirements of diverse tasks. Based on this principle, we design a new general image restoration backbone network, X-Restormer. Extensive experiments demonstrate that X-Restormer possesses good task generality and achieves state-of-the-art performance across a variety of tasks.

1 Introduction

Image restoration aims to generate high-quality images from degraded images. In recent years, deep learning has achieved great success in this field, with numerous networks being proposed to address various image restoration tasks. Initially, networks are primarily designed to solve specific restoration tasks and are typically validated only on selected tasks. As deep learning techniques have continued to evolve, there has been an increasing focus on the development of general-purpose networks that can be applied to a broad range of tasks. This trend is particularly evident in the high-level vision field, where new backbone networks are being designed to support multiple tasks (He et al. 2016; Liu et al. 2021), including classification, detection and segmentation. For image restoration, although more and more restoration backbones can handle multiple restoration tasks, their task generality is still limited, as illustrated in Figure 1. For instance, SwinIR (Liang et al. 2021) achieves state-of-the-art performance on image super-resolution (SR) but falls short on image deblurring and dehazing. Conversely, Restormer (Zamir et al. 2022) performs exceptionally well

* equal contribution.

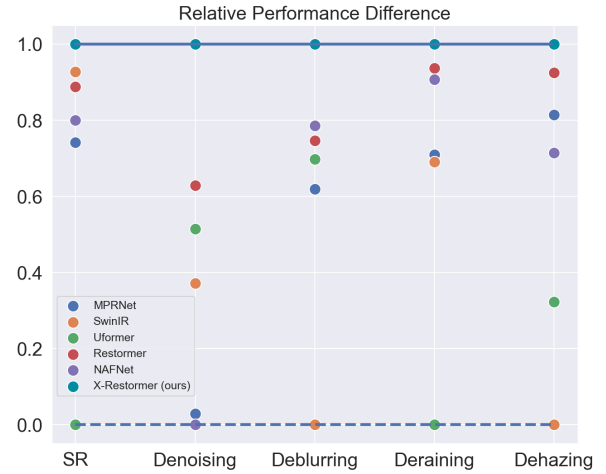


Figure 1: Relative performance difference of different backbone networks on five image restoration tasks¹. These representative networks exhibit diverse performance on these tasks, while our method presents superior task generality.

on image dehazing and deraining but is less effective on image SR. This discrepancy can be attributed to the fact that the characteristics of image degradation vary across different image restoration tasks. While all image restoration tasks involve mapping degraded images to clean images, the requirements for the capability of backbone networks differ depending on the specific task.

Designing a general image restoration backbone network presents a significant challenge. However, the development of such a network holds considerable value, as it has the potential to greatly reduce costs associated with research and application. To achieve this goal, we first conduct a comparative study of mainstream backbone networks on the representative tasks, including image SR, denoising, deblurring, deraining and dehazing. These five tasks are chosen due to the distinct characteristics of their degrada-

¹We set the minimum mean performance on test sets in Table 2 of the task (i) as the lower bound $P_{lower}^{(i)}$, and the performance of X-Restormer as the upper bound $P_{upper}^{(i)}$. The ordinate of each point with performance $P^{(i)}$ is calculated as $(P^{(i)} - P_{lower}^{(i)}) / P_{upper}^{(i)}$.

tion and the considerable variation in the performance of existing methods. Five representative backbone networks are selected in the study, including MPRNet (Zamir et al. 2021), Uformer (Wang et al. 2022b), SwinIR (Liang et al. 2021), Restormer (Zamir et al. 2022) and NAFNet (Chen et al. 2022). These five networks encompass classic architectures such as U-shape encoder-decoder architecture, plain residual-in-residual architecture and multi-stage progressive architecture. They also employ several common operators, including convolution, spatial self-attention and transposed self-attention (Zamir et al. 2022). We benchmark the five representative methods on the selected five tasks. The experimental results clearly reflect the performance disparity of different backbone networks on different tasks. We then conduct a detailed analysis of the characteristics of these tasks and these backbone networks to explain the reasons behind the performance differences. Based on the comparative study, we believe that a general backbone network must be highly comprehensive in terms of functionality that meets the diverse needs of various tasks.

It is noteworthy that Restormer stands out in the comparative study. It outperforms almost all other methods in four tasks and is only inferior to SwinIR in the SR task. Restormer’s U-shape architecture allows it to process large-size inputs. The network employs transposed self-attention with channel-wise feature maps as tokens, facilitating global receptive field mapping. Moreover, the network incorporates numerous depth-wise convolutions, promoting spatial information interaction. Functionally, Restormer integrates nearly all the capabilities of other compared networks, demonstrating relatively good task generality. However, its inferior performance in SR compared to SwinIR indicates its limitation in spatial information interaction. We believe that this is due to the weaker spatial mapping ability of depth-wise convolution compared to spatial self-attention (i.e., window-based self-attention in SwinIR). To mitigate this limitation, we introduce spatial self-attention into Restormer by alternately replacing half of the transposed self-attention block with overlapping cross-attention block (Chen et al. 2023b). This straightforward modification markedly improve the performance of Restormer without increasing the number of parameters. Experiments show that the enhanced network, X-Restormer, obtains state-of-the-art performance on all five tasks with the best task generality.

Our main contributions can be summarized as follows:

- We conduct a comparative study by constructing an image restoration benchmark, highlighting the challenges faced by existing backbone networks in task generality.
- Based on the benchmark results, we perform a detailed analysis of the characteristics of different degradations and different networks. We emphasize that the general backbone network design must meet the functional requirements of different restoration tasks.
- By further enhancing the spatial mapping ability of Restormer, we design a preliminary general backbone network, X-Restormer. Without additional parameters, X-Restormer achieves significant performance improvement and exhibits superior task generality.

2 Related Work

Image restoration networks. Since SRCNN (Dong et al. 2014) first introduces deep learning to image SR and obtains superior performance over conventional methods, numerous deep networks have been proposed for various image restoration tasks such as image SR (Lim et al. 2017; Zhang et al. 2018b; Chen et al. 2023b), denoising (Zhang et al. 2017a,b; Wang et al. 2022b), deblurring (Abuolaim and Brown 2020; Chen et al. 2021b), deraining (Yang et al. 2017a; Chen et al. 2021a; Liu et al. 2022), dehazing (Yang et al. 2017b; Tu et al. 2022; Song et al. 2023). In earlier years, most deep networks are designed for specific image restoration tasks. For instance, (Zhang et al. 2018a) uses channel attention mechanism to construct a CNN-based SR network. (Zhang, Zuo, and Zhang 2018) builds a denoising network by inputting multiple downsampled sub-images and a noise level map. (Fu et al. 2017a) utilizes residual connections to for a deraining network. (Cai et al. 2016) estimates the transmission rate and inverts the atmospheric scattering model using a CNN to achieve image dehazing. (Nah, Hyun Kim, and Mu Lee 2017) designs a multi-scale network for image deblurring. Recently, more and more methods have been developed to tackle multiple image restoration tasks. (Zamir et al. 2021) builds a multi-stage CNN for deraining, deblurring and denoising. (Wang et al. 2022b) designs a U-shape Transformer for deraining, deblurring and denoising. (Liang et al. 2021) implements a Swin Transformer-based network that achieves state-of-the-art performance on SR, denoising and compression artifact reduction. (Zamir et al. 2022) proposes a novel transposed self-attention to build a U-shape network for deraining, deblurring and denoising. (Chen et al. 2022) constructs a U-shaped CNN for denoising and deblurring.

Difference from the previous network design research.

While previous works have proposed networks that excel in various image restoration tasks, their primary focus is on constructing stronger networks to achieve performance breakthroughs in specific tasks. In contrast, this work pays more attention to the task generality of the backbone network, possessing a vision different from previous works. More specifically, our objective is to explore the design principles and directions of general image restoration networks. We are not seeking to create powerful networks for peak performance on a single or some specific tasks, but rather to ensure satisfactory performance across a diverse range of tasks. Regarding the concrete implementation, we do not intend to construct complex network architectures or modules. Our preference, rather, is to enhance task generality through the use of the simplest methodology available.

There are concurrent works that propose advanced networks for image restoration tasks. DAT (Chen et al. 2023c) combines spatial-window self-attention and channel-wise self-attention to handle image SR. IPT-V2 (Li et al. 2023) designs a spatial-channel Transformer block to build the network and obtains the winner award in the NTIRE 2023 image denoising challenge (Li et al. 2023). However, the motivation and specific network implementation details of our work are distinct from these studies.

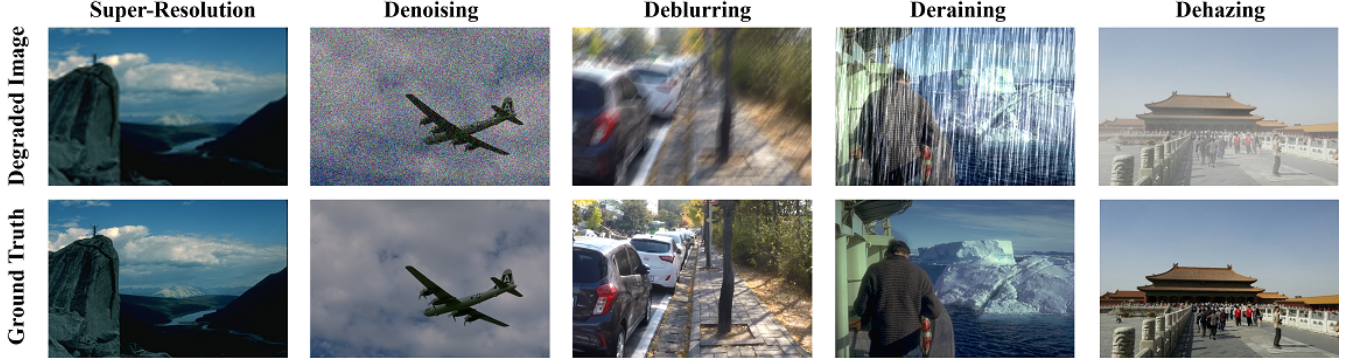


Figure 2: Selected five image restoration tasks. The degradation in each task vary significantly.

3 Image Restoration Benchmark

In this section, we first briefly introduce several image restoration tasks, each with its own representative degradation characteristics. Subsequently, we classify mainstream image restoration networks based on two key aspects: architecture and core operator. On this basis, we select five representative networks and conduct a benchmark experiment across five different tasks. We describe the experimental setup and explain its rationality. Finally, we present the benchmark results and conduct a detailed analysis of them.

3.1 Image Restoration Tasks

We introduce five representative tasks selected for the benchmark experiments. Figure 2 shows examples of these tasks. These tasks are chosen for two primary reasons. First, they represent very common restoration tasks. Second, and more importantly, the degradation characteristics of these tasks vary significantly. As such, they provide a robust means of evaluating the task generality of an image restoration backbone network. To further illustrate this point, we provide a brief overview of the degradation associated with each task.

Let I_{GT} denote the ground truth image and I_{LQ} denote the degraded image, where $I_{GT} \in \mathbb{R}^{H \times W \times 3}$. The degradation model of classic image SR can be represented as:

$$I_{LQ} = (I_{GT} \otimes k) \downarrow_s, \quad (1)$$

where $I_{LQ} \in \mathbb{R}^{\frac{H}{s} \times \frac{W}{s} \times 3}$ represents the low-resolution image. k denotes the bicubic downsampling kernel and \downarrow_s represents the downscaling factor. This degradation process is strongly related to local information and there is a significant loss of information.

The degradation model of image denoising can be denoted as:

$$I_{LQ} = I_{GT} + n, \quad (2)$$

where $n \in \mathbb{R}^{H \times W \times 3}$ represents the noise map. For Gaussian denoising, these noise values are content-independent.

The degradation model of image deblurring (for motion deblurring) can be denoted as:

$$I_{LQ} = \sum_t (f_{motion}^t(I_{GT})), \quad (3)$$

where $f_{motion}^t(\cdot)$ represents the motion function of the image under different continuous exposure times. This degradation is related to the global motion offset of the image.

The degradation model of image deraining can be simply denoted as:

$$I_{LQ} = I_{GT} + R, \quad (4)$$

where R denotes the additive rain streak, simulated by the physics models, such as (Li et al. 2016; Liu et al. 2018a). The difference between this degradation and Gaussian noise is that the added R is not evenly distributed on the image and has a correlation with the image content.

The degradation model of image dehazing, based on the atmospheric scattering model, can be denoted as:

$$I_{LQ} = I_{GT} * t(I_{GT}) + A(1 - t(I_{GT})), \quad (5)$$

where $t(\cdot)$ represents the transmission function and $t(I_{GT})$ is related to the distance from the scene point to the camera. Thus, this degradation is related to the depth information of the image. Overall, it can be seen that these image restoration tasks deal with completely different degradations.

3.2 Image Restoration Networks

Mainstream networks for image restoration can be categorized into three types of architectures: U-shape encoder-decoder, plain residual-in-residual, and multi-stage progressive. Schematic diagrams of these architectures are provided in *Supp*. The U-shape encoder-decoder architecture is commonly employed in various image restoration network. It performs multiple downsampling and upsampling of features, allowing it to effectively process multi-scale features. Besides, this architecture can quickly expand the network's receptive field and effectively save computational costs. U-shape backbone networks include MWCNN (Liu et al. 2018b) and Uformer (Wang et al. 2022b) and etc. The multi-stage architecture divides the entire network into several sub-networks and progressively processes features. Common networks based on this architecture include MPRNet (Zamir et al. 2021) and HINet (Chen et al. 2021b), which are primarily used for image deraining and deblurring. The plain residual-in-residual architecture is originally designed for image SR, so backbone networks based on

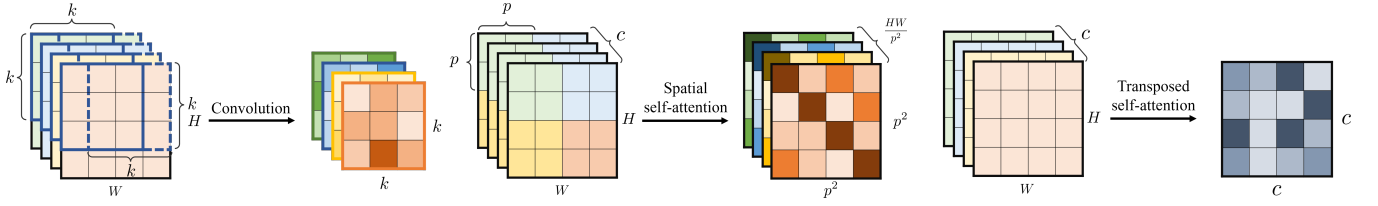


Figure 3: The core operators in image restoration networks.

Table 1: Architectures and core operators of the five selected backbone networks for the image restoration benchmark.

Network	Architecture	Core operator
MPRNet	Multi-Stage	Convolution
Uformer	U-Shape	Spatial self-attention
SwinIR	Plain residual-in-residual	Spatial self-attention
Restormer	U-Shape	Transposed self-attention
NAFNet	U-Shape	Convolution

this architecture often have unique advantages on SR, like SwinIR (Liang et al. 2021).

The core operators for constructing an image restoration network can be categorized into three main types: convolution, spatial self-attention, and transposed self-attention. As shown in Figure 3, the convolution operator calculates a fixed-size filter and processes the entire feature map through a sliding window. Many backbone networks are built entirely on convolution like RDN (Zhang et al. 2020). Spatial self-attention is typically implemented as window self-attention in image restoration tasks. It calculates the attention matrix within a fixed window size, generating content-aware weights that are functionally similar to a large kernel dynamic filter. This operator has strong local fitting ability and is particularly advantageous on SR (Chen et al. 2023a). Transposed self-attention is a recently proposed operator that calculates the attention matrix based on the channel, treating the entire feature map of each channel as a token. This operator has a global receptive field. When combined with depth-wise convolution, it demonstrates superiority in multiple restoration tasks (Zamir et al. 2022).

The selected five representative backbone networks for the benchmark experiment encompass the abovementioned architectures and core operators, as presented in Table 1.

3.3 Experimental Settings

For image SR, we conduct experiments on upscaling factor $\times 4$. We use the DF2K dataset (the same as SwinIR (Liang et al. 2021)) to train models. Low-resolution images are generated from the ground truth images using bicubic down-sampling in MATLAB. For U-shape networks, we first up-sample the input low-resolution images through bilinear interpolation. The performance is reported on the Y channel. For denoising, we adopt the DFWB dataset for training. Noisy images are generated by adding Gaussian noise with a noise level of 50. For deblurring, we use the motion deblurring dataset GoPro (Nah, Hyun Kim, and Mu Lee 2017) to train the models. For deraining, we conduct experiments

using the synthetic rain dataset Rain13K and calculate the performance on the Y channel, following Restormer (Zamir et al. 2022). For dehazing, we use the indoor training set (ITS) of the RESIDE dataset (Li et al. 2018), the same as (Song et al. 2023).

To maximize the capability of these networks, we use the official codes and training configurations provided by different methods to train the models¹. Note that all models are trained without using any pre-training strategy (e.g., $\times 2$ pre-training for SR) or special tricks (e.g., EMA in SwinIR and TLC in NAFNet) for fair comparison. In addition, we find that different methods may not use exactly the same test sets and the same metrics calculation in their papers to report performance. Therefore, we retest all models based on exactly the same data and calculate PSNR/SSIM using the popular open-source toolbox BasicSR (Wang et al. 2022a).

3.4 Benchmark Results

We present the quantitative results for each task on benchmark test sets in Table 2. (Due to space constraints, complete results are provided in *Supp.*) Several important observations can be made from the benchmark results: 1) Different networks exhibit varying performance on different tasks. For instance, Uformer excels in denoising and deblurring tasks but performs poorly in deraining and super-resolution tasks. SwinIR performs best on SR but worst in deblurring and dehazing tasks. 2) Networks with U-shaped and multi-stage architectures demonstrate clear advantages in deblurring and dehazing tasks. 3) MPRNet and NAFNet, which are based on convolutional operators, exhibit moderate performance across all tasks without outstanding results. 4) SwinIR, which employs plain architecture and spatial self-attention operators, outperforms other networks by a significant margin in SR. 5) Restormer performs best in almost all tasks except for SR, where it is weaker than SwinIR. For dehazing, Restormer far outperforms other methods.

3.5 Analysis

We explain the above observations by analyzing the degradation characteristics of different tasks and the characteristics of different backbone networks. For the SR task, its degradation lies in the compression of local information, resulting in a large loss of high-frequency details. Therefore, SR networks often require stronger local mapping ca-

¹We have also tried to train all networks with a unified configuration, but find it unreasonable. The performance of networks may vary greatly with different training configurations and optimization strategies, making it hard to determine a fair unified setting.

Table 2: Quantitative results of the benchmark. The best and second-best performance results are in **bold** and underline.

Method	SR		Denoising		Deblurring		Deraining		Dehazing
	Set14	Urban100	CBS68	Urban100	GoPro	HIDE	Test100	Rain100H	SOTS Indoor
MPRNet	28.90/0.7889	26.88/0.8081	28.48/0.8087	29.71/0.8847	32.66/0.9392	30.96/0.9188	30.29/0.8983	30.43/0.8905	<u>40.34/0.9936</u>
SwinIR	29.07/0.7944	27.47/0.8258	28.56/0.8118	29.88/0.8861	31.66/0.9209	29.41/0.8957	30.05/0.8996	30.45/0.8952	29.14/0.9676
Uformer	27.14/0.7398	25.60/0.7651	28.55/ 0.8130	29.98/0.8900	<u>33.05/0.9417</u>	30.89/0.9203	27.93/0.8910	24.06/0.8454	33.58/0.9856
Restormer	29.06/0.7934	27.32/0.8199	28.60/0.8130	30.02/0.8898	32.92/0.9398	31.22/0.9226	32.03/0.9237	31.48/0.9054	41.87/0.9938
NAFNet	29.03/0.7919	27.00/0.8112	28.52/0.8098	29.65/0.8840	33.08/0.9419	31.22/0.9237	<u>30.33/0.9097</u>	32.83/0.9135	38.97/0.9928

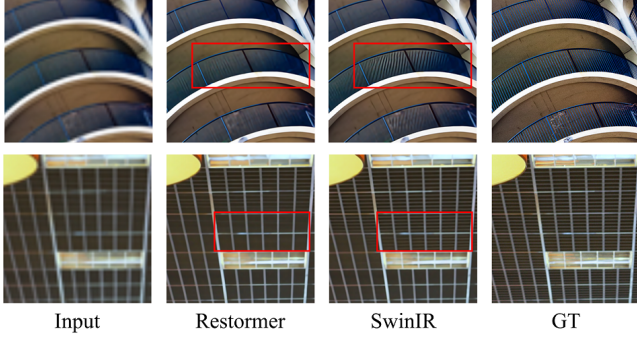


Figure 4: Visual comparison of Restormer with SwinIR.

pability, or even generative capability. The U-shaped architecture, which involves multiple downsampling operations, intuitively increases the difficulty of feature reconstruction. In contrast, the window self-attention mechanism in SwinIR has been shown to have a stronger local fitting ability than convolution (Chen et al. 2023b). As a result, SwinIR, which is based on a plain structure and employs spatial self-attention operators, has a clear advantage in SR.

Denoising involves smoothing the image to eliminate high-frequency noise and integrating low-frequency information to reconstruct a clear image. We conjecture that Restormer’s high performance in denoising can be attributed to its ability to better smooth noise through channel-based processing, which is similar to operating in the frequency domain. In contrast, SwinIR performs well due to the strong reconstruction ability of its local self-attention mechanism.

Deblurring (specifically for motion blur here) involves addressing global motion shifts in the image. As a result, the use of global or multi-scale information is intuitively necessary for the deblurring network. Thus, networks based on a U-shape architecture perform well on this task. In contrast, SwinIR, which focuses more on local information processing, performs poorly on deblurring.

Similar results can be observed for dehazing. Due to the involvement of global depth information in the haze model, the ability to use large-scale features is important. Besides, dehazing networks process the low-frequency transformations of the image, such as color and contrast, which is a processing of global information.

Deraining is relatively unique, as rain is unevenly distributed in images and there are significant differences between different rain drops and streaks. Therefore, there is no clear pattern in the performance of different backbone networks for deraining. Nevertheless, Restormer still performs relatively better than others.

Based on the above analysis, it is evident that the principle of designing a general backbone network should be to ensure that the network can fulfill the requirements of all tasks for network functions. The results indicate that Restormer has exceptional task generality. It can be attributed to several factors: 1) Restormer’s U-shape architecture enables the network to accommodate larger input sizes and efficiently process multi-scale information. 2) Transposed self-attention allows for direct interaction with global information. 3) The presence of depth-wise convolution enables the network to process spatial information effectively. In summary, due to Restormer’s comprehensive functionality, it is capable of meeting the needs of almost all tasks.

4 General Backbone Network Design

Based on the results and analysis of the benchmark, we select Restormer as a start point for designing a more general backbone network. Our initial analysis reveals that the primary limitation of Restormer is its weak spatial mapping ability. To address this issue, we simply introduce spatial self-attention into Restormer, resulting in a new general backbone network for image restoration.

Weakness of Restormer. We attribute the weakness of Restormer to its limited spatial mapping ability. This is evident in its subpar performance in the SR task, as well as inferior visual quality. As depicted in Figure 4, although Restormer can directly utilize global information, it fails to reconstruct fine textures even for self-repeated patterns, while SwinIR is capable of doing so. To overcome this limitation, we incorporate a spatial self-attention module into Restormer to design a more powerful backbone network.

Network structure. In Figure 5, we present our proposed backbone network, denoted as X-Restormer. To fuse shallow and deep features, skip connections are incorporated into the architecture. In contrast to Restormer, we replace half of the transposed self-attention blocks (TSAB) with spatial self-attention blocks (SSAB). Given an input feature F_{in} , the two blocks process it alternately as follows:

$$F_t = F_{in} + TSA(LN(F_{in})), \quad (6)$$

$$F_{t,out} = F_t + FFN(LN(F_t)), \quad (7)$$

$$F_s = F_{t,out} + SSA(LN(F_{t,out})), \quad (8)$$

$$F_{out} = F_s + FFN(LN(F_s)), \quad (9)$$

where F_t , $F_{t,out}$, F_s and $F_{s,out}$ represent the intermediate feature in TSAB, the output of TSAB, the intermediate feature in SSAB and the output of SSAB, respectively. F_{out} means the output of the two consecutive blocks, and also

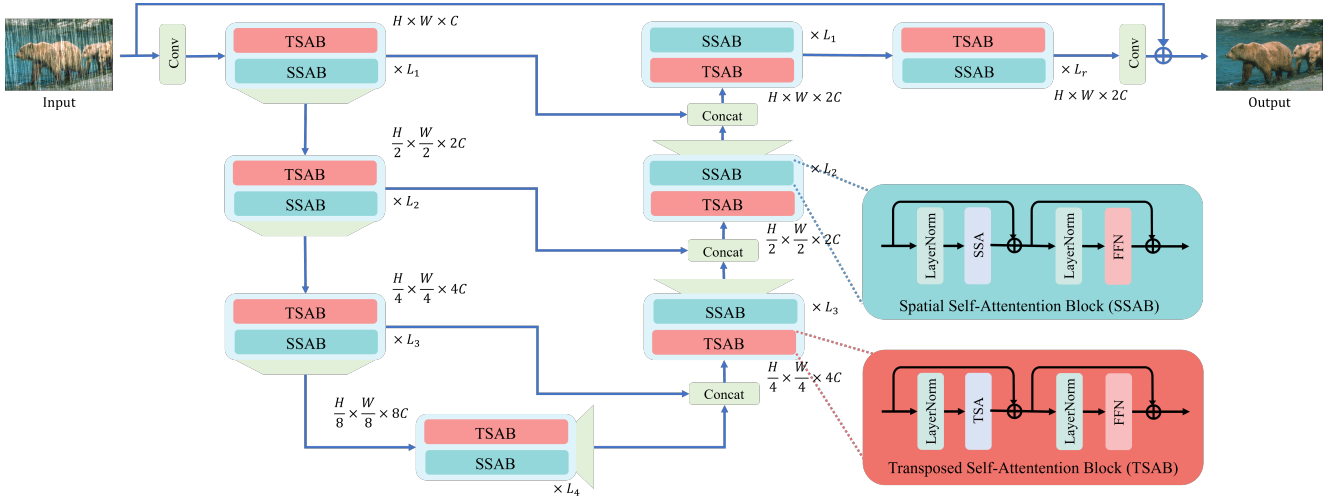


Figure 5: The network structure of the proposed X-Restormer. In order to enhance the spatial mapping ability of Restormer and create a more general backbone network, we replace half of the transposed self-attention blocks in Restormer with spatial self-attention blocks. For TSA, we retain the preliminary multi-Dconv head transposed attention (MDTA) used in Restormer. For SSA, we adopt the overlapping cross-attention (OCA) in HAT (Chen et al. 2023b).

serves as the input for the following two blocks. $TSA(\cdot)$ and $SSA(\cdot)$ indicate transposed self-attention (TSA) and spatial self-attention (SSA) module. $LN(\cdot)$ denotes the LayerNorm operation and $FFN(\cdot)$ represents the feed-forward network.

Specially, we adopt the Multi-Dconv Transpose Attention (MDTA) as the TSA module. It first generates *query* (Q), *key* (K) and *value* (V) by applying 1×1 convolutions followed by 3×3 depth-wise convolutions. Then, the channel attention matrix of size $\mathbb{R}^{C \times C}$ is calculated by the dot-product of reshaped Q and K followed by a Softmax function. The schematic of TSA is shown in Figure 3. Finally, the result is generated by the dot-product of the attention matrix and V . For SSA, we adopt the Overlapping Cross-Attention (OCA) introduced in the HAT model (Chen et al. 2023b). We choose this approach because the shifted window mechanism is not suitable for our consecutive blocks, and HAT demonstrates the effectiveness of OCA. For the calculation of OCA, Q is produced by partitioning the input into non-overlapping windows, while K and V are generated by partitioning the input into overlapping windows with a manually set overlapping size. Apart from the different window partition methods, the calculation of OCA is essentially identical to that of standard window self-attention. For FFN, we employ the Gated-Dconv Feed-forward Network (GDFN) architecture, as used in Restormer. Instead of using two 1×1 convolutions to construct a MLP, GDFN first processes input features through two 3×3 depth-wise convolutions and 1×1 convolutions. Then, the resulting features are combined via element-wise multiplication and passes through another 1×1 convolution to produce the final output.

We emphasize that our design of X-Restormer is not to develop novel architectures or modules for the network to improve the performance of some specific tasks, but to enhance the task generality of the network according to the principle of our general backbone network design through as simple means as possible.

5 Experiments

5.1 Experimental Setup

We conduct experiments for the proposed X-Restormer on the same datasets used in the benchmark experiment, including DF2K for x4 SR, DFWB for denoising with noise level $\sigma = 50$, Gopro for deblurring, Rain13K for deraining, and ITS for dehazing. We implement the same network hyperparameters and training strategy for all five image restoration tasks. Specifically, X-Restormer employs a 4-level encoder-decoder with three times down-sampling and up-sampling. To maintain a similar number of parameters as the original Restormer, from level-1 to level-4, the numbers of consecutive blocks (containing a TSAB and a SSAB) are [2, 4, 4, 4], attention heads in TSA and SSA are both [1, 2, 4, 8], and channel numbers are [48, 96, 192, 384]. The channel expansion factor in GDFN is 2.66. The overall parameters are 26.06M, slightly less than Restormer of 26.13M. To optimize the models, we employ the AdamW optimizer with $\beta_1 = 0.9$ and $\beta_2 = 0.99$, utilizing an initial learning rate of $3e^{-4}$. The learning rate decay follows a cosine scheduler with intervals at 92k and 208k iterations, and the total training iterations are 300K. For all five tasks, the input patch size is set to 256×256 and the batch size is set to 32. For data augmentation, we use horizontal and vertical flips. We utilize the $L1$ loss function to train models for all the tasks. Notably, we do not adopt any training tricks (e.g., $\times 2$ SR pretraining or EMA strategy) or testing tricks (e.g., TLC).

5.2 Experimental Results

We compare our X-Restormer with the top three models in the benchmark experiments (based on the same test configurations) as well as other state-of-the-art approaches (based on the reported performance in their papers) in this section.

Image SR. In Table 3, we present the quantitative results of $\times 4$ SR on five benchmark datasets: Set5 (Bevilac-

Table 3: Quantitative results on $\times 4$ image SR. The best and second-best performance results are in **bold** and underline. * means the SwinIR model is pre-trained on $\times 2$ SR.

Model	Set5 PSNR/SSIM	Set14 PSNR/SSIM	BSD100 PSNR/SSIM	Urban100 PSNR/SSIM	Manga109 PSNR/SSIM
RCAN	32.63/0.9002	28.87/0.7889	27.77/0.7436	26.82/0.8087	31.22/0.9173
RCAN-it	32.69/0.9007	28.99/0.7922	27.87/0.7459	27.16/0.8168	31.78/0.9217
SwinIR*	32.92/0.9044	<u>29.09/0.7950</u>	27.92/0.7489	27.45/0.8254	<u>32.03/0.9260</u>
IPT	32.64/-	29.01/-	27.82/-	27.26/-	-/-
EDT	32.82/0.9031	29.09/0.7939	27.91/0.7483	27.46/0.8246	32.05/0.9254
NAFNet	32.79/0.9010	29.03/0.7919	27.86/0.7463	27.00/0.8112	31.77/0.9216
SwinIR	32.88/0.9041	29.07/0.7944	<u>27.93/0.7490</u>	<u>27.47/0.8258</u>	31.96/0.9255
Restormer	<u>32.94/0.9039</u>	29.06/0.7934	27.91/0.7482	27.32/0.8199	31.96/0.9244
X-Restormer	33.16/0.9058	29.17/0.7963	28.00/0.7512	27.66/0.8291	32.38/0.9279

Table 5: Quantitative results on deblurring. The best and second-best performance results are in **bold** and underline.

Model	GoPro PSNR/SSIM	HIDE PSNR/SSIM	RealBlur-R PSNR/SSIM	RealBlur-J PSNR/SSIM
SPAIR	32.06/0.953	30.29/0.931	-/-	28.81/0.875
MIMO-UNet+	32.45/0.957	29.99/0.930	35.54/0.947	27.63/0.837
IPT	32.52/-	-/-	-/-	-/-
MPRNet	32.66/0.959	30.96/0.939	35.99/0.952	28.70/0.873
Uformer	33.05/0.942	30.89/0.920	36.19/0.956	29.09/0.886
NAFNet	33.08/0.942	31.22/0.924	35.97/0.952	28.32/0.857
Restormer	32.92/0.940	31.22/0.923	36.19/0.957	28.96/0.879
X-Restormer	33.44/0.946	31.76/0.930	36.27/0.958	28.87/0.878

Table 7: Quantitative results on image dehazing. The best and second-best performance results are in **bold** and underline.

Model	PFDN PSNR/SSIM	FFA-Net PSNR/SSIM	AECR-Ne PSNR/SSIM	MAXIM PSNR/SSIM	DehazeFormer PSNR/SSIM	MPRNet PSNR/SSIM	NAFNet PSNR/SSIM	Restormer PSNR/SSIM	X-Restormer PSNR/SSIM
SOTS Indoor	32.68/0.976	36.39/0.989	37.17/0.990	39.72/-	40.05/0.996	40.34/0.994	38.97/0.994	41.97/0.994	42.90/0.995

qua et al. 2012), Set14 (Zeyde, Elad, and Protter 2010), BSD100 (Martin et al. 2001a), Urban100 (Huang, Singh, and Ahuja 2015a) and Manga109 (Matsui et al. 2017). The state-of-the-art approaches, including RCAN (Zhang et al. 2018a), RCAN-it (Lin et al. 2022), SwinIR (Niu et al. 2020), IPT (Chen et al. 2021a) and EDT (Li et al. 2021) are compared in this experiment. As shown in the results, X-Restormer significantly outperforms Restormer by 0.22dB on Set5, 0.34dB on Urban100 and 0.42dB on Manga109. This demonstrates the effectiveness of our design in enhancing the spatial mapping ability of Restormer. Furthermore, X-Restormer surpasses the SOTA method EDT by 0.2dB on Urban100 and 0.35dB on Manga109, indicating the effectiveness of X-Restormer on SR. Despite this, we point out that our method still cannot beat the most powerful SR approaches, such as HAT. We believe that in terms of the SR task, the plain residual in residual architecture designed for SR is still more efficient.

Image denoising. In Table 4, we provide the quantitative results of Gaussian denoising with the noise level $\sigma = 50$ on four benchmark datasets: CBSD68 (Martin et al. 2001b), Kodak24 (Franzen 1999), McMaster (Zhang et al. 2011) and Urban100 (Huang, Singh, and Ahuja 2015a). The state-of-the-art methods: FFDNet (Zhang, Zuo, and Zhang 2018), RNAN (Zhang et al. 2019), RDN (Zhang et al. 2020), IPT (Chen et al. 2021a) and DRUNet (Zhang et al. 2021) are compared in this experiment. As one can see that X-Restormer achieves the state-of-the-art performance, surpassing SwinIR by 0.36dB and outperforming Restormer by

Table 4: Quantitative results on image denoising with the Gaussian noise level $\sigma = 50$. The best and second-best performance results are in **bold** and underline.

Model	CBSD68 PSNR/SSIM	Kodak24 PSNR/SSIM	McMaster PSNR/SSIM	Urban100 PSNR/SSIM
FFDNet	27.96/-	28.98/-	29.18/-	28.05/-
RNAN	28.27/-	29.58/-	29.72/-	29.08/-
RDN	28.31/-	29.66/-	-/-	29.38/-
IPT	28.39/-	29.64/-	29.98/-	29.71/-
DRUNet	28.51/-	29.86/-	30.08/-	29.61/-
SwinIR	28.56/0.8118	29.95/0.8221	30.20/0.8489	29.88/0.8861
Uformer	28.55/0.8130	29.97/0.8244	30.16/0.8485	29.98/0.8900
Restormer	<u>28.60/0.8130</u>	<u>30.01/0.8237</u>	<u>30.30/0.8517</u>	<u>30.02/0.8898</u>
X-Restormer	28.63/0.8138	30.05/0.8245	30.33/0.8518	30.24/0.8928

Table 6: Quantitative results on image deraining. The best and second-best performance results are in **bold** and underline.

Model	Test100 PSNR/SSIM	Rain100H PSNR/SSIM	Rain100L PSNR/SSIM	Test1200 PSNR/SSIM	Test2800 PSNR/SSIM
PreNet	24.81/0.851	26.77/0.858	32.44/0.950	31.36/0.911	31.75/0.916
MSPFN	27.50/0.876	28.66/0.860	32.40/0.933	32.39/0.916	32.82/0.930
MPRNet	30.27/0.897	30.41/0.890	36.40/0.965	32.91/0.916	33.64/0.938
SPAIR	30.35/0.909	30.95/0.892	36.93/0.969	<u>33.04/0.922</u>	33.34/0.936
SwinIR	30.05/0.900	30.45/0.895	37.00/0.969	30.49/0.893	33.63/0.940
NAFNet	30.33/0.910	32.83/0.914	36.96/0.971	32.58/0.922	32.15/0.933
Restormer	32.03/0.924	31.48/0.905	39.08/0.979	33.22/0.927	34.21/0.945
X-Restormer	32.21/0.927	<u>32.09/0.914</u>	<u>39.10/0.978</u>	32.31/0.919	<u>33.93/0.945</u>

0.22dB on Urban100. This demonstrates the superiority of X-Restormer on image denoising.

Image deblurring. We conduct experiments on motion deblurring and compare the performance of our X-Restormer with the models in the benchmark dataset, as well as several state-of-the-art motion deblurring methods, including SPAIR (Purohit et al. 2021), MIMO-UNet+ (Cho et al. 2021), IPT (Chen et al. 2021a) and MPRNet (Zamir et al. 2021). The performance is evaluated on four benchmark datasets, comprising both synthetic datasets (GoPro (Nah, Hyun Kim, and Mu Lee 2017) and HIDE (Shen et al. 2019)) and real-world datasets (RealBlur-R and RealBlur-J (Rim et al. 2020)). As shown in Table 5, our X-Restormer achieves large performance gains over the other models on synthetic datasets, with an improvement of 0.36dB on GoPro compared to NAFNet and 0.54dB on HIDE compared to Restormer. Besides, X-Restormer obtains the SOTA performance on RealBlur-R and considerable performance on RealBlur-J, showing the effectiveness of our method on real-world motion deblurring scenarios.

Image deraining. We perform image deraining experiments and evaluate the performance of our X-Restormer against the models in the benchmark experiment and the state-of-the-art image deraining methods, including PreNet (Ren et al. 2019), MSPFN (Jiang et al. 2020), MPRNet (Zamir et al. 2021) and SPAIR (Purohit et al. 2021). The evaluation is conducted on five benchmark datasets: Test100 (Huang, Singh, and Ahuja 2015b), Rain100L (Yang

et al. 2017c), Rain100H(Yang et al. 2017c), Test1200(Zhang and Patel 2018) and Test2800(Fu et al. 2017b). As indicated in Table 6, X-Restormer outperforms the other models on Test100, Rain100H and Rain100L but performs inferior to Restormer on Test1200 and Test2800. This discrepancy is caused by the variations in degradation produced by different rain models. Nonetheless, our X-Restormer model exhibits comparable performance to state-of-the-art methods, demonstrating its effectiveness on image deraining.

Image dehazing. We conduct experiments on image dehazing and compare the performance of our proposed X-Restormer model with the selected models in the benchmark experiment, as well as several state-of-the-art dehazing methods, including PFDN (Dong and Pan 2020), FFA-Net (Yang et al. 2017b), AECR-Net (Wu et al. 2021), MAXIM (Tu et al. 2022) and DehazeFormer (Song et al. 2023). The evaluation is performed on the benchmark dataset SOTS Indoor (Li et al. 2018), with results presented in Table 7. Notably, our X-Restormer model significantly outperforms Restormer by a large margin of 0.93dB. When compared to the state-of-the-art dehazing method DehazeFormer, our X-Restormer model achieves a breakthrough performance gain of 2.85dB. These results demonstrate the superiority of our proposed method for image dehazing.

Summary. We can observe that the performance of Restormer is significantly improved after its spatial mapping capability has been enhanced. Specifically, X-Restormer obtains large performance gains against Restormer of 0.42dB (Manga109), 0.22dB (Urban100), 0.54dB (HIDE), 0.61dB (Rain100H) and 0.93dB (SOTS Indoor) on image SR, denoising, deblurring, deraining and dehazing, demonstrating the effectiveness of our design. Moreover, on all these five tasks, our X-Restormer obtains state-of-the-art performance, which is not achieved by previous networks. Despite its simplicity, X-Restormer clearly has better task generality than other methods. We hope it can inspire more works on the general image restoration backbone network design.

6 Conclusion

In this paper, we conduct a comparative study of existing image restoration backbone networks to design a general backbone network. We first select representative image restoration tasks based on their distinct degradation characteristics. Subsequently, we classify existing image restoration backbone networks from two aspects: architecture and core operators, to select representative networks for our research. Five representative image restoration backbone networks are chosen for the benchmark experiment across the selected five tasks. The benchmark results indicate that comprehensive functionality is crucial for designing a general image restoration backbone network. Consequently, we select Restormer, which demonstrates superior average performance in the comparative study, for further improvement. To improve the task generality of Restormer, we introduce spatial self-attention into it to enhance the spatial mapping capability. Experimental results show that the designed X-Restormer achieves significant performance improvement and demonstrates the best task generality.

References

- Abuolaim, A.; and Brown, M. S. 2020. Defocus deblurring using dual-pixel data. In *Computer Vision—ECCV 2020: 16th European Conference, Glasgow, UK, August 23–28, 2020, Proceedings, Part X 16*, 111–126. Springer. 2
- Bevilacqua, M.; Roumy, A.; Guillemot, C.; and Alberi-Morel, M. L. 2012. Low-complexity single-image super-resolution based on nonnegative neighbor embedding. 6
- Cai, B.; Xu, X.; Jia, K.; Qing, C.; and Tao, D. 2016. Dehazenet: An end-to-end system for single image haze removal. *IEEE transactions on image processing*, 25(11): 5187–5198. 2
- Chen, H.; Wang, Y.; Guo, T.; Xu, C.; Deng, Y.; Liu, Z.; Ma, S.; Xu, C.; Xu, C.; and Gao, W. 2021a. Pre-trained image processing transformer. In *Proceedings of the IEEE/CVF Conference on Computer Vision and Pattern Recognition*, 12299–12310. 2, 7
- Chen, L.; Chu, X.; Zhang, X.; and Sun, J. 2022. Simple baselines for image restoration. *arXiv preprint arXiv:2204.04676*. 2, 11
- Chen, L.; Lu, X.; Zhang, J.; Chu, X.; and Chen, C. 2021b. Hinet: Half instance normalization network for image restoration. In *Proceedings of the IEEE/CVF Conference on Computer Vision and Pattern Recognition*, 182–192. 2, 3, 11
- Chen, X.; Wang, X.; Zhang, W.; Kong, X.; Qiao, Y.; Zhou, J.; and Dong, C. 2023a. HAT: Hybrid Attention Transformer for Image Restoration. *arXiv preprint arXiv:2309.05239*. 4
- Chen, X.; Wang, X.; Zhou, J.; Qiao, Y.; and Dong, C. 2023b. Activating more pixels in image super-resolution transformer. In *Proceedings of the IEEE/CVF Conference on Computer Vision and Pattern Recognition*, 22367–22377. 2, 5, 6, 11
- Chen, Z.; Zhang, Y.; Gu, J.; Kong, L.; Yang, X.; and Yu, F. 2023c. Dual Aggregation Transformer for Image Super-Resolution. In *Proceedings of the IEEE/CVF International Conference on Computer Vision*, 12312–12321. 2
- Cho, S.-J.; Ji, S.-W.; Hong, J.-P.; Jung, S.-W.; and Ko, S.-J. 2021. Rethinking coarse-to-fine approach in single image deblurring. In *Proceedings of the IEEE/CVF international conference on computer vision*, 4641–4650. 7
- Dong, C.; Loy, C. C.; He, K.; and Tang, X. 2014. Learning a deep convolutional network for image super-resolution. In *European conference on computer vision*, 184–199. Springer. 2
- Dong, J.; and Pan, J. 2020. Physics-Based Feature Dehazing Networks. In Vedaldi, A.; Bischof, H.; Brox, T.; and Frahm, J.-M., eds., *Computer Vision – ECCV 2020*, 188–204. Cham: Springer International Publishing. ISBN 978-3-030-58577-8. 8
- Franzen, R. 1999. Kodak lossless true color image suite. source: <http://r0k.us/graphics/kodak>, 4(2). 7
- Fu, X.; Huang, J.; Zeng, D.; Huang, Y.; Ding, X.; and Paisley, J. 2017a. Removing rain from single images via a deep detail network. In *Proceedings of the IEEE conference on computer vision and pattern recognition*, 3855–3863. 2

- Fu, X.; Huang, J.; Zeng, D.; Huang, Y.; Ding, X.; and Paisley, J. 2017b. Removing rain from single images via a deep detail network. In *Proceedings of the IEEE conference on computer vision and pattern recognition*, 3855–3863. 8
- He, K.; Zhang, X.; Ren, S.; and Sun, J. 2016. Deep residual learning for image recognition. In *Proceedings of the IEEE conference on computer vision and pattern recognition*, 770–778. 1
- Huang, J.-B.; Singh, A.; and Ahuja, N. 2015a. Single image super-resolution from transformed self-exemplars. In *Proceedings of the IEEE conference on computer vision and pattern recognition*, 5197–5206. 7
- Huang, J.-B.; Singh, A.; and Ahuja, N. 2015b. Single image super-resolution from transformed self-exemplars. In *Proceedings of the IEEE conference on computer vision and pattern recognition*, 5197–5206. 7
- Jiang, K.; Wang, Z.; Yi, P.; Chen, C.; Huang, B.; Luo, Y.; Ma, J.; and Jiang, J. 2020. Multi-scale progressive fusion network for single image deraining. In *Proceedings of the IEEE/CVF conference on computer vision and pattern recognition*, 8346–8355. 7
- Li, B.; Ren, W.; Fu, D.; Tao, D.; Feng, D.; Zeng, W.; and Wang, Z. 2018. Benchmarking single-image dehazing and beyond. *IEEE Transactions on Image Processing*, 28(1): 492–505. 4, 8
- Li, W.; Lu, X.; Qian, S.; Lu, J.; Zhang, X.; and Jia, J. 2021. On efficient transformer-based image pre-training for low-level vision. *arXiv preprint arXiv:2112.10175*. 7
- Li, Y.; Tan, R. T.; Guo, X.; Lu, J.; and Brown, M. S. 2016. Rain streak removal using layer priors. In *Proceedings of the IEEE conference on computer vision and pattern recognition*, 2736–2744. 3
- Li, Y.; Zhang, Y.; Timofte, R.; Van Gool, L.; Tu, Z.; Du, K.; Wang, H.; Chen, H.; Li, W.; Wang, X.; et al. 2023. NTIRE 2023 challenge on image denoising: Methods and results. In *Proceedings of the IEEE/CVF Conference on Computer Vision and Pattern Recognition*, 1904–1920. 2
- Liang, J.; Cao, J.; Sun, G.; Zhang, K.; Van Gool, L.; and Timofte, R. 2021. Swinir: Image restoration using swin transformer. In *Proceedings of the IEEE/CVF International Conference on Computer Vision*, 1833–1844. 1, 2, 4, 11
- Lim, B.; Son, S.; Kim, H.; Nah, S.; and Mu Lee, K. 2017. Enhanced deep residual networks for single image super-resolution. In *Proceedings of the IEEE conference on computer vision and pattern recognition workshops*, 136–144. 2
- Lin, Z.; Garg, P.; Banerjee, A.; Magid, S. A.; Sun, D.; Zhang, Y.; Van Gool, L.; Wei, D.; and Pfister, H. 2022. Revisiting RCAN: Improved Training for Image Super-Resolution. 7
- Liu, J.; Yang, W.; Yang, S.; and Guo, Z. 2018a. Erase or fill? deep joint recurrent rain removal and reconstruction in videos. In *Proceedings of the IEEE conference on computer vision and pattern recognition*, 3233–3242. 3
- Liu, L.; Xie, L.; Zhang, X.; Yuan, S.; Chen, X.; Zhou, W.; Li, H.; and Tian, Q. 2022. Tape: Task-agnostic prior embedding for image restoration. In *European Conference on Computer Vision*, 447–464. Springer. 2
- Liu, P.; Zhang, H.; Zhang, K.; Lin, L.; and Zuo, W. 2018b. Multi-level wavelet-CNN for image restoration. In *Proceedings of the IEEE conference on computer vision and pattern recognition workshops*, 773–782. 3
- Liu, Z.; Lin, Y.; Cao, Y.; Hu, H.; Wei, Y.; Zhang, Z.; Lin, S.; and Guo, B. 2021. Swin transformer: Hierarchical vision transformer using shifted windows. In *Proceedings of the IEEE/CVF International Conference on Computer Vision*, 10012–10022. 1
- Martin, D.; Fowlkes, C.; Tal, D.; and Malik, J. 2001a. A database of human segmented natural images and its application to evaluating segmentation algorithms and measuring ecological statistics. In *Proceedings Eighth IEEE International Conference on Computer Vision. ICCV 2001*, volume 2, 416–423. IEEE. 7
- Martin, D.; Fowlkes, C.; Tal, D.; and Malik, J. 2001b. A database of human segmented natural images and its application to evaluating segmentation algorithms and measuring ecological statistics. In *Proceedings Eighth IEEE International Conference on Computer Vision. ICCV 2001*, volume 2, 416–423. IEEE. 7
- Matsui, Y.; Ito, K.; Aramaki, Y.; Fujimoto, A.; Ogawa, T.; Yamasaki, T.; and Aizawa, K. 2017. Sketch-based manga retrieval using manga109 dataset. *Multimedia Tools and Applications*, 76(20): 21811–21838. 7
- Nah, S.; Hyun Kim, T.; and Mu Lee, K. 2017. Deep multi-scale convolutional neural network for dynamic scene deblurring. In *Proceedings of the IEEE conference on computer vision and pattern recognition*, 3883–3891. 2, 4, 7
- Niu, B.; Wen, W.; Ren, W.; Zhang, X.; Yang, L.; Wang, S.; Zhang, K.; Cao, X.; and Shen, H. 2020. Single image super-resolution via a holistic attention network. In *Computer Vision–ECCV 2020: 16th European Conference, Glasgow, UK, August 23–28, 2020, Proceedings, Part XII 16*, 191–207. Springer. 7
- Purohit, K.; Suin, M.; Rajagopalan, A.; and Boddeti, V. N. 2021. Spatially-adaptive image restoration using distortion-guided networks. In *Proceedings of the IEEE/CVF International Conference on Computer Vision*, 2309–2319. 7
- Ren, D.; Zuo, W.; Hu, Q.; Zhu, P.; and Meng, D. 2019. Progressive image deraining networks: A better and simpler baseline. In *Proceedings of the IEEE/CVF conference on computer vision and pattern recognition*, 3937–3946. 7
- Rim, J.; Lee, H.; Won, J.; and Cho, S. 2020. Real-world blur dataset for learning and benchmarking deblurring algorithms. In *Computer Vision–ECCV 2020: 16th European Conference, Glasgow, UK, August 23–28, 2020, Proceedings, Part XXV 16*, 184–201. Springer. 7
- Shen, Z.; Wang, W.; Lu, X.; Shen, J.; Ling, H.; Xu, T.; and Shao, L. 2019. Human-aware motion deblurring. In *Proceedings of the IEEE/CVF International Conference on Computer Vision*, 5572–5581. 7
- Song, Y.; He, Z.; Qian, H.; and Du, X. 2023. Vision transformers for single image dehazing. *IEEE Transactions on Image Processing*, 32: 1927–1941. 2, 4, 8

- Tu, Z.; Talebi, H.; Zhang, H.; Yang, F.; Milanfar, P.; Bovik, A.; and Li, Y. 2022. MAXIM: Multi-Axis MLP for Image Processing. *CVPR*. 2, 8
- Wang, X.; Xie, L.; Yu, K.; Chan, K. C.; Loy, C. C.; and Dong, C. 2022a. BasicSR: Open Source Image and Video Restoration Toolbox. <https://github.com/XPiPixelGroup/BasicSR>. 4, 11
- Wang, Z.; Cun, X.; Bao, J.; Zhou, W.; Liu, J.; and Li, H. 2022b. Uformer: A general u-shaped transformer for image restoration. In *Proceedings of the IEEE/CVF Conference on Computer Vision and Pattern Recognition*, 17683–17693. 2, 3, 11
- Wu, H.; Qu, Y.; Lin, S.; Zhou, J.; Qiao, R.; Zhang, Z.; Xie, Y.; and Ma, L. 2021. Contrastive learning for compact single image dehazing. In *Proceedings of the IEEE/CVF Conference on Computer Vision and Pattern Recognition*, 10551–10560. 8
- Yang, W.; Tan, R. T.; Feng, J.; Liu, J.; Guo, Z.; and Yan, S. 2017a. Deep joint rain detection and removal from a single image. In *Proceedings of the IEEE conference on computer vision and pattern recognition*, 1357–1366. 2
- Yang, W.; Tan, R. T.; Feng, J.; Liu, J.; Guo, Z.; and Yan, S. 2017b. Deep joint rain detection and removal from a single image. In *Proceedings of the IEEE conference on computer vision and pattern recognition*, 1357–1366. 2, 8
- Yang, W.; Tan, R. T.; Feng, J.; Liu, J.; Guo, Z.; and Yan, S. 2017c. Deep joint rain detection and removal from a single image. In *Proceedings of the IEEE conference on computer vision and pattern recognition*, 1357–1366. 7, 8
- Zamir, S. W.; Arora, A.; Khan, S.; Hayat, M.; Khan, F. S.; and Yang, M.-H. 2022. Restormer: Efficient transformer for high-resolution image restoration. In *Proceedings of the IEEE/CVF Conference on Computer Vision and Pattern Recognition*, 5728–5739. 1, 2, 4, 11
- Zamir, S. W.; Arora, A.; Khan, S.; Hayat, M.; Khan, F. S.; Yang, M.-H.; and Shao, L. 2021. Multi-stage progressive image restoration. In *Proceedings of the IEEE/CVF conference on computer vision and pattern recognition*, 14821–14831. 2, 3, 7, 11
- Zeyde, R.; Elad, M.; and Protter, M. 2010. On single image scale-up using sparse-representations. In *International conference on curves and surfaces*, 711–730. Springer. 7
- Zhang, H.; and Patel, V. M. 2018. Density-aware single image de-raining using a multi-stream dense network. In *Proceedings of the IEEE conference on computer vision and pattern recognition*, 695–704. 8
- Zhang, K.; Li, Y.; Zuo, W.; Zhang, L.; Van Gool, L.; and Timofte, R. 2021. Plug-and-play image restoration with deep denoiser prior. *IEEE Transactions on Pattern Analysis and Machine Intelligence*, 44(10): 6360–6376. 7
- Zhang, K.; Zuo, W.; Chen, Y.; Meng, D.; and Zhang, L. 2017a. Beyond a gaussian denoiser: Residual learning of deep cnn for image denoising. *IEEE transactions on image processing*, 26(7): 3142–3155. 2
- Zhang, K.; Zuo, W.; Gu, S.; and Zhang, L. 2017b. Learning deep CNN denoiser prior for image restoration. In *Proceedings of the IEEE conference on computer vision and pattern recognition*, 3929–3938. 2
- Zhang, K.; Zuo, W.; and Zhang, L. 2018. FFDNet: Toward a fast and flexible solution for CNN-based image denoising. *IEEE Transactions on Image Processing*, 27(9): 4608–4622. 2, 7
- Zhang, L.; Wu, X.; Buades, A.; and Li, X. 2011. Color demosaicking by local directional interpolation and nonlocal adaptive thresholding. *Journal of Electronic imaging*, 20(2): 023016–023016. 7
- Zhang, Y.; Li, K.; Li, K.; Wang, L.; Zhong, B.; and Fu, Y. 2018a. Image super-resolution using very deep residual channel attention networks. In *Proceedings of the European conference on computer vision (ECCV)*, 286–301. 2, 7, 11
- Zhang, Y.; Li, K.; Li, K.; Zhong, B.; and Fu, Y. 2019. Residual non-local attention networks for image restoration. *arXiv preprint arXiv:1903.10082*. 7
- Zhang, Y.; Tian, Y.; Kong, Y.; Zhong, B.; and Fu, Y. 2018b. Residual dense network for image super-resolution. In *Proceedings of the IEEE conference on computer vision and pattern recognition*, 2472–2481. 2, 11
- Zhang, Y.; Tian, Y.; Kong, Y.; Zhong, B.; and Fu, Y. 2020. Residual dense network for image restoration. *IEEE transactions on pattern analysis and machine intelligence*, 43(7): 2480–2495. 4, 7

A Comparative Study of Image Restoration Networks for General Backbone Network Design

Supplementary Material

Xiangyu Chen^{1,2,3 *} Zheyuan Li^{3 *} Yuandong Pu^{2,4 *} Yihao Liu²
Jiantao Zhou¹ Yu Qiao^{2,3} Chao Dong^{2,3}

¹University of Macau ²Shanghai Artificial Intelligence Laboratory
³Shenzhen Institute of Advanced Technology, CAS ⁴Shanghai Jiao Tong University
<https://github.com/Andrew0613/X-Restormer>

Abstract

In the supplementary material, we present additional experiments and results to complement the main manuscript. First, we illustrate details about schematic diagrams of mentioned three kinds of **architectures**. Second, we provide complete **benchmark results** for the five image restoration tasks. Third, **visual results** of X-Restormer and benchmark networks are presented. Fourth, we conduct an **ablation study** to further verify the effectiveness of our X-Restormer. Finally, we provide the **model complexity comparison** of our X-Restormer with Restormer.

Architecture Investigation

In the realm of image restoration networks, prevailing architectures fall into three distinct categories, as depicted in Figure 6: (a) plain residual-in-residual, (b) U-shaped encoder-decoder and (c) multi-stage progressive architectures. The plain residual-in-residual design emerges as the most prevalent choice for the SR task, originating with RCAN (Zhang et al. 2018a). In this architecture, the features of the original input size are deeply mapped through multiple residual groups. Each residual group contains multiple residual blocks. Eminent examples encompass RDN (Zhang et al. 2018b) and SwinIR (Liang et al. 2021). The U-shaped encoder-decoder architecture excels at extracting multi-scale features while maintaining efficiency through the utilization of down-sampled features. The advantage of this architecture is that it can accept large-size inputs and the receptive field grows rapidly. Representative models include Uformer (Wang et al. 2022b), NAFNet (Chen et al. 2022), Restormer (Zamir et al. 2022). Our X-Restormer also employ this architecture. The multi-stage architecture involves multiple inputs of the degraded image, subsequently arranging UNet architectures in a serial stack, as seen in the case of MPRNet (Zamir et al. 2021) and HINet (Chen et al. 2021b). The multi-stage architecture introduces extra connections between various-sized feature maps that result in much intra-block complexity (Chen et al. 2022).

Complete Benchmark Results

We provide the complete the benchmark results on image SR, denoising, deblurring, deraining and dehazing, as shown in Table 8, Table 9, Table 10, Table 11 and Table 12. Since different methods may not use exactly the same data and calculation ways in their papers, we uniformly calculate the performance using BasicSR toolbox (Wang et al. 2022a) on the totally the same test data for fair comparison.

Visual Comparison

We present the visual comparison of the benchmark results with the proposed X-Restormer on image SR, denoising, deblurring, deraining and dehazing, as depicted in Figure 7, Figure 8, Figure 9, Figure 10, Figure 11, respectively.

Ablation Study

We conduct ablation study to explore the effectiveness of our design for X-Restormer. For fast validation, experiments are implemented on image SR and deblurring, based on a small variant of X-Restormer with the numbers of consecutive blocks of [1,2,2,4], the channel numbers of [36, 72, 144, 288] (total 10.62M parameters) and the input patch size of 192×192 . We first explore the impact of cascade and parallel connections of transposed self-attention block (TSAB) and spatial self-attention block (SSAB). Then, we compare the effects of standard window self-attention (WSA) and the overlapping cross-attention (OCA) for the choice of SSA.

Cascade or Parallel. In Table 13, we show the quantitative results on image SR and deblurring for the cascade and parallel connections of TSAB and SSAB. As one can see that the model using cascade design obtains much better performance on all benchmark datasets. Thus, our X-Restormer uses cascade connection for TSAB and SSAB.

Effectiveness of OCA. In Table 14, we provide the quantitative comparison of standard non-overlapping window self-attention (WSA) with the used overlapping self-attention (OCA) for the choice of spatial self-attention in X-Restormer. The overlapping size is set to 0.5, the same as HAT (Chen et al. 2023b). We can see that OCA performs better than WSA. Therefore, we adopt OCA in X-Restormer.

Model Complexity Comparison

In Table 15, we present the model complexity comparison of our X-Restormer with Restormer on image SR and motion deblurring. With similar number of parameters and a relatively larger computational complexity, X-Restormer obtains significant performance improvement over Restormer. We also provide a small variant of X-Restormer, denoted as X-Restormer-s, by reducing the original dimension to 44. With fewer parameters and similar FLOPs (calculated for 256×256 output), X-Restormer-s can also perform much better than Restormer.

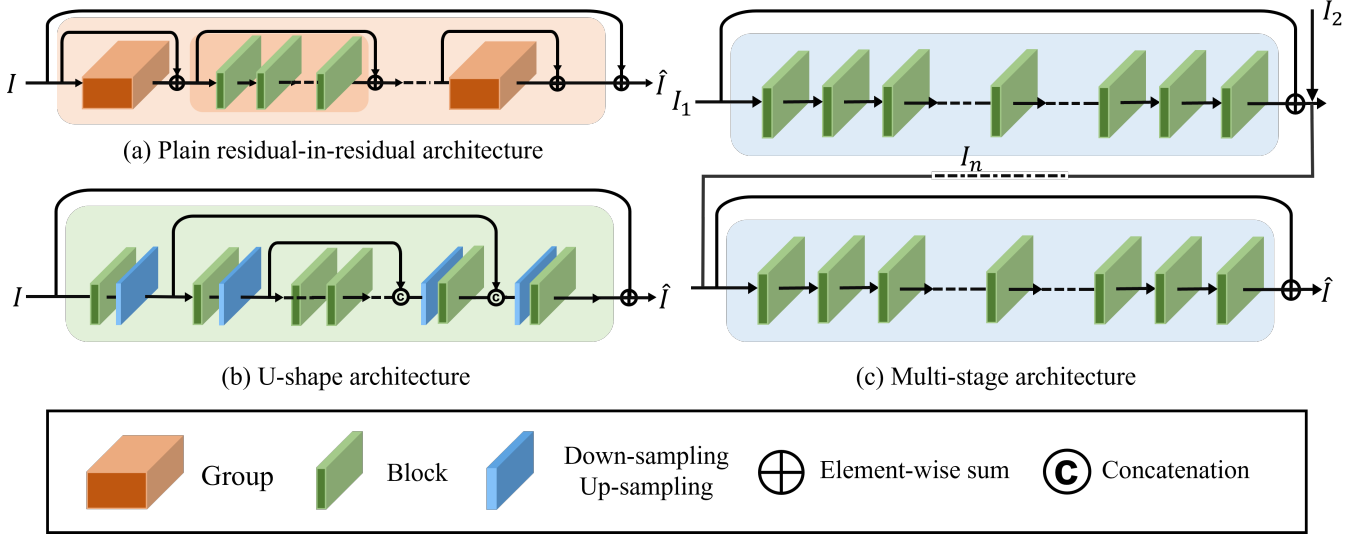


Figure 6: Three different architectures of image restoration backbone networks.

Table 8: Benchmark results on $\times 4$ image SR. The best and second-best performance results are in **bold** and underline.

Model	Set5 PSNR/SSIM	Set14 PSNR/SSIM	BSD100 PSNR/SSIM	Urban100 PSNR/SSIM	Manga109 PSNR/SSIM
MPRNet	32.57/0.8996	28.90/0.7889	27.78/0.7425	26.88/0.8081	31.44/0.9182
SwinIR	<u>32.88/0.9041</u>	29.07/0.7944	27.93/0.7490	27.47/0.8258	31.96/0.9255
Uformer	30.25/0.8665	27.14/0.7398	27.67/0.7475	25.60/0.7651	31.69/0.9233
NAFNet	32.79/0.9010	29.03/0.7919	27.86/0.7463	27.00/0.8112	<u>31.77/0.9216</u>
Restormer	32.94/0.9039	<u>29.06/0.7934</u>	<u>27.91/0.7482</u>	<u>27.32/0.8199</u>	31.96/0.9244

Table 9: Benchmark results on image denoising with the Gaussian noise level $\sigma = 50$.

Model	CBSD68 PSNR/SSIM	Kodak24 PSNR/SSIM	McMaster PSNR/SSIM	Urban100 PSNR/SSIM
MPRNet	28.48/0.8087	29.86/0.8193	30.04/0.8447	29.71/0.8847
SwinIR	<u>28.56/0.8118</u>	29.95/0.8221	<u>30.20/0.8489</u>	29.88/0.8861
Uformer	28.55/0.8130	<u>29.97/0.8244</u>	30.16/0.8485	<u>29.98/0.8900</u>
NAFNet	28.52/0.8098	29.90/0.8204	30.07/0.8455	29.65/0.8840
Restormer	28.60/0.8130	30.01/0.8237	30.30/0.8517	<u>30.02/0.8898</u>

Table 10: Benchmark results on motion deblurring.

Model	GoPro PSNR/SSIM	HIDE PSNR/SSIM	RealBlur-R PSNR/SSIM	RealBlur-J PSNR/SSIM
MPRNet	32.66/0.939	30.96/0.919	35.99/0.952	28.70/0.873
SwinIR	31.66/0.921	29.41/0.896	35.49/0.947	27.55/0.840
Uformer	33.05/0.942	30.89/0.920	36.19/0.956	29.09/0.886
NAFNet	33.08/0.942	31.22/0.924	35.97/0.952	28.32/0.857
Restormer	<u>32.92/0.940</u>	<u>31.22/0.923</u>	36.19/0.957	<u>28.96/0.879</u>

Table 11: Benchmark results on image deraining.

Model	Test100 PSNR/SSIM	Rain100H PSNR/SSIM	Rain100L PSNR/SSIM	Test1200 PSNR/SSIM	Test2800 PSNR/SSIM
MPRNet	30.29/0.898	30.43/0.891	36.46/0.966	32.94/0.914	<u>33.66/0.939</u>
SwinIR	30.05/0.900	30.45/0.895	<u>37.00/0.969</u>	30.49/0.893	33.63/0.940
Uformer	27.93/0.891	24.06/0.845	35.96/0.965	<u>32.75/0.919</u>	28.22/0.913
NAFNet	<u>30.33/0.910</u>	32.83/0.914	36.96/0.971	<u>32.58/0.922</u>	32.15/0.933
Restormer	32.03/0.924	<u>31.48/0.905</u>	39.08/0.979	33.22/0.927	34.21/0.945

Table 12: Benchmark results on image dehazing.

Model	MPRNet PSNR/SSIM	SwinIR PSNR/SSIM	Uformer PSNR/SSIM	NAFNet PSNR/SSIM	Restormer PSNR/SSIM
SOTS Indoor	<u>40.34/0.994</u>	29.14/0.968	33.58/0.986	38.97/0.993	41.97/0.994

Table 13: Ablation study on the connection ways.

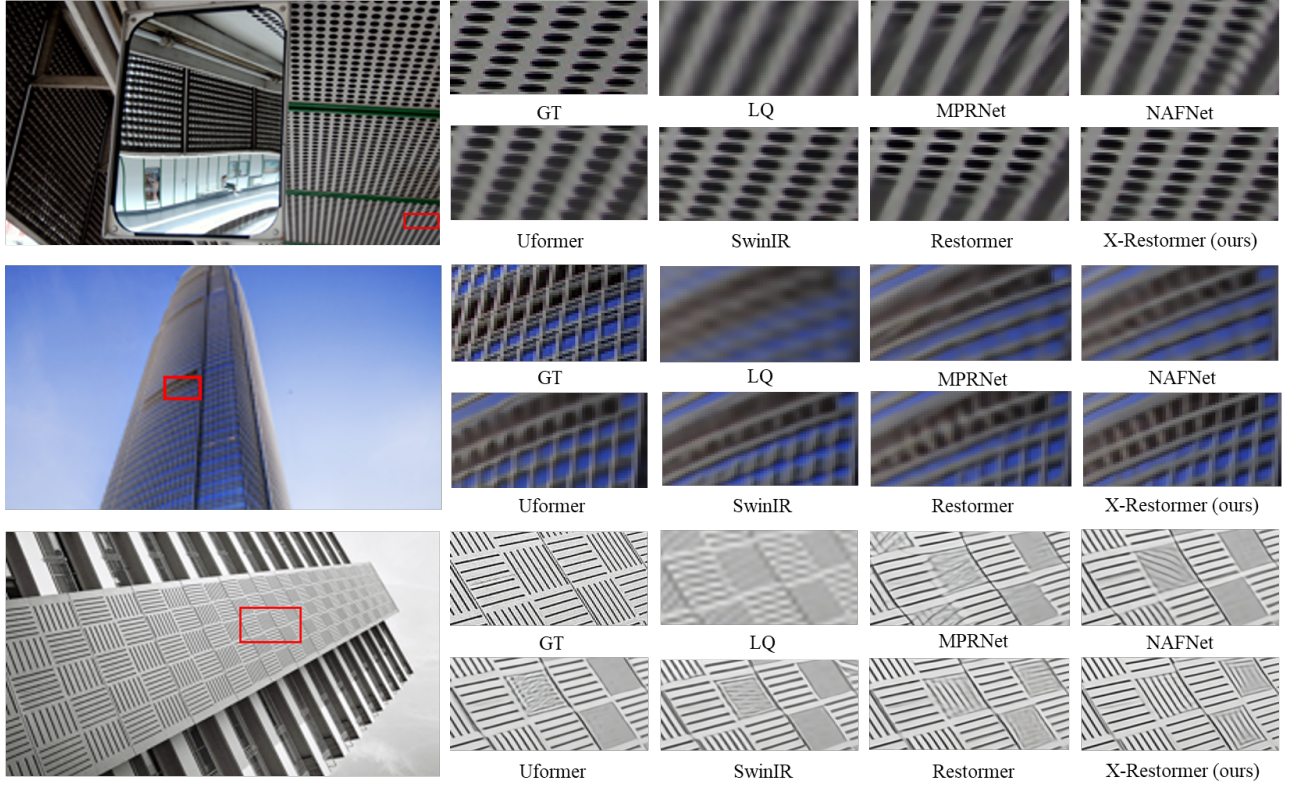
Model	Set5 PSNR/SSIM	Set14 PSNR/SSIM	BSD100 PSNR/SSIM	Urban100 PSNR/SSIM	Manga109 PSNR/SSIM	GoPro PSNR/SSIM	HIDE PSNR/SSIM	RealBlur-R PSNR/SSIM	RealBlur-J PSNR/SSIM
Parallel	32.61/0.9002	28.92/0.7902	27.78/0.7440	26.85/0.8083	31.36/0.9190	31.53/0.9222	29.67/0.9016	36.12/0.9553	28.95/0.8792
Cascade(ours)	32.82/0.9023	29.05/0.7925	27.85/0.7461	27.17/0.8158	31.77/0.9204	32.25/0.9316	30.50/0.9136	36.24/0.9572	28.92/0.8808

Table 14: Ablation study on the choice of SSA.

Model	Set5 PSNR/SSIM	Set14 PSNR/SSIM	BSD100 PSNR/SSIM	Urban100 PSNR/SSIM	Manga109 PSNR/SSIM	GoPro PSNR/SSIM	HIDE PSNR/SSIM	RealBlur-R PSNR/SSIM	RealBlur-J PSNR/SSIM
WSA	32.81/0.9021	29.01/0.7914	27.82/0.7453	27.09/0.8138	31.68/0.9203	32.09/0.9295	30.41/0.9129	36.24/0.9570	29.00/0.8822
OCA(ours)	32.82/0.9021	29.05/0.7927	27.86/0.7464	27.19/0.8162	31.80/0.9209	32.25/0.9316	30.50/0.9136	36.24/0.9572	28.92/0.8808

Table 15: Model Complexity Comparison. FLOPs are calculated for 256×256 output.

Model	Params(M)	FLOPs(G)	Set5 PSNR/SSIM	Set14 PSNR/SSIM	BSD100 PSNR/SSIM	Urban100 PSNR/SSIM	Manga109 PSNR/SSIM	GoPro PSNR/SSIM	HIDE PSNR/SSIM	RealBlur-R PSNR/SSIM	RealBlur-J PSNR/SSIM
Restormer	26.1	141.0	32.94/0.9039	29.06/0.7934	27.91/0.7482	27.32/0.8199	31.96/0.9244	32.92/0.9419	31.22/0.9226	36.19/0.9571	28.96/0.8785
X-Restormer-s	22.3	140.9	33.04/0.9047	29.18/0.7963	27.97/0.7505	27.63/0.8287	32.37/0.9256	33.41/0.9452	31.52/0.9277	36.24/0.9572	28.75/0.8730
X-Restormer	26.0	164.3	33.16/0.9058	29.17/0.7963	28.00/0.7512	27.66/0.8291	32.38/0.9279	33.44/0.9459	31.76/0.9299	36.27/0.9581	28.87/0.8780

Figure 7: Visual comparison on $\times 4$ image SR.

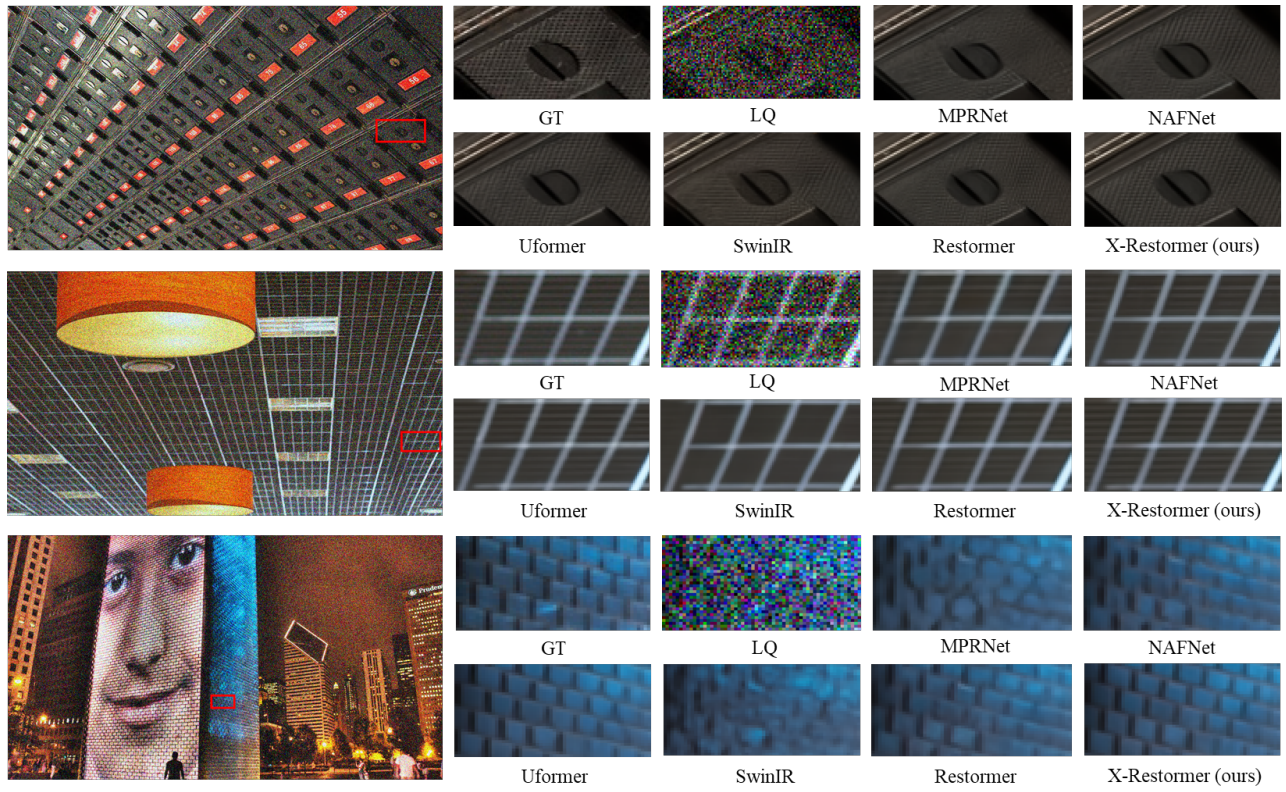


Figure 8: Visual comparison on image denoising with the Gaussian noise level $\sigma = 50$.



Figure 9: Visual comparison on motion deblurring.

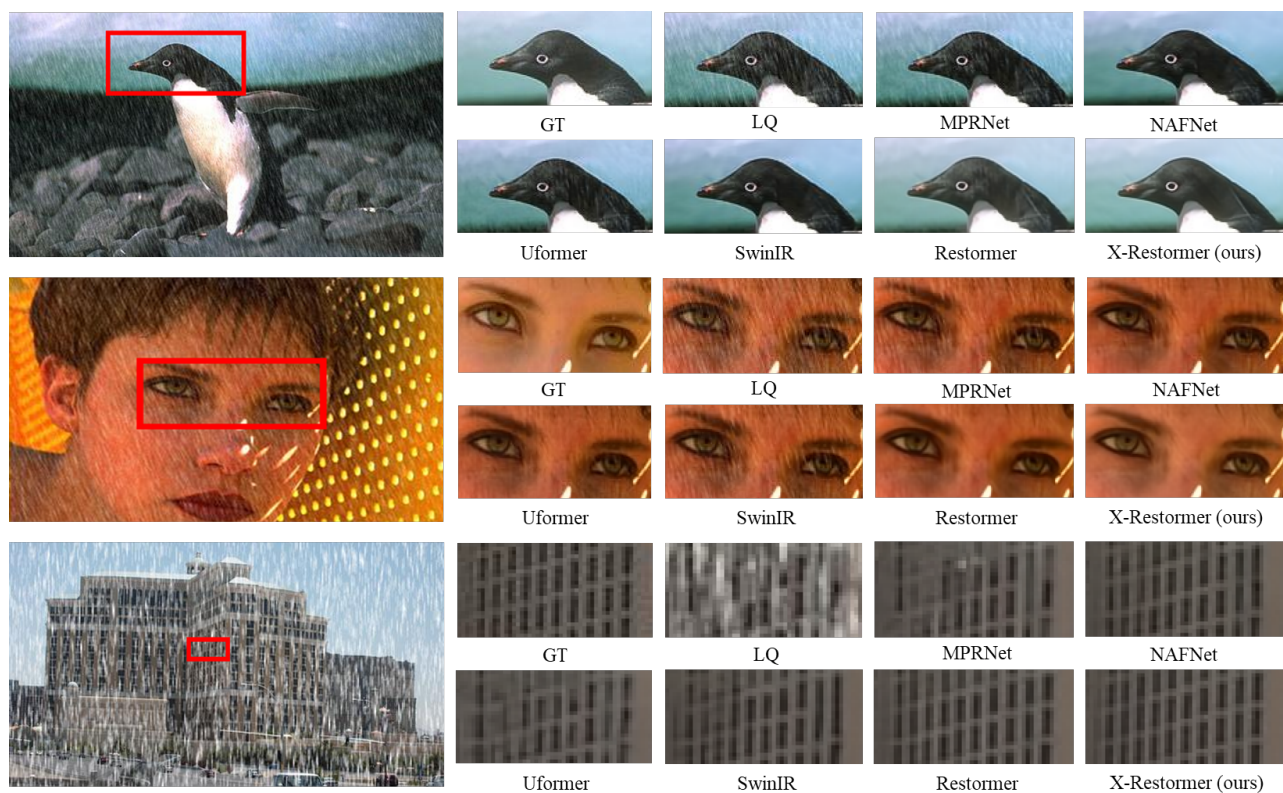


Figure 10: Visual comparison on image deraining.



Figure 11: Visual comparison on image dehazing.